

## Monte Carlo simulation of the shapes of domains in phospholipid monolayers

M. A. Mayer and T. K. Vanderlick\*

*Department of Chemical Engineering, University of Pennsylvania, Philadelphia, Pennsylvania 19104-6393*

(Received 4 June 1996)

The dispersed domains which result from phase separation in phospholipid monolayers have long been known to exhibit complex and intriguing geometries. Over the last decade, much work has gone into the theoretical prediction of these shapes using energy minimization calculations. While such studies have provided much insight into the behavior of domain shapes, they ignore the effect of entropy and thus are truly applicable only as the temperature approaches absolute zero. In this paper, we present a Monte Carlo approach for the prediction of domain shapes through simulation, thereby introducing temperature as an explicit parameter. Where applicable, results from this simulation are compared to prior shape calculations and to experimental results. We find that the first order transition predicted between circular and bilobed domains applies only at low temperature. Moreover, we find that bilobed domains should only be found when the domain elongation occurs slowly; rapid elongation produces multiple branched domains. Finally, we find that the width of these branches in elongated domains is independent of both the number of branches and the size of the domain. [S1063-651X(97)01701-7]

PACS number(s): 02.70.-c, 68.10.-m

### I. INTRODUCTION

It has been known for some time that insoluble phospholipid monolayers at the air-water interface exhibit intriguing geometries during phase transitions [1–3]. One of the more outstanding features of these geometries is the shapes taken by individual domains of the higher density phase. While many of the observed domain shapes clearly result from growth kinetics [4], these same domains typically evolve into a final shape characteristic of the particular lipid or lipid mixture being examined. Moreover, stable domain shapes appear to be a reproducible function of the state of the monolayer [1] and domain size. It should be noted that at least three other systems exhibit domain morphologies similar to phospholipid monolayers: ferromagnetic fluids confined between parallel plates [5–7], thin magnetic films [8], and superconducting films [9,10]. Presumably, this similarity arises from the fact that each of these systems is composed of a field of parallel oriented dipoles, either electrostatic or magnetostatic.

In recent years, much work has been undertaken in the prediction of stable domain shapes and the transitions between stable shapes as governed by the competition between dipolar repulsion and interfacial tension. The majority of these studies can be categorized into three basic strategies: (1) direct comparison of the energies of predetermined shapes (or shape classes) [11–14], (2) analysis of the stability of predetermined shapes [15,16], and (3) dynamic evolution of shape as driven by the energy gradient [5,17]. The first two methods, however, are only capable of predicting shapes explicitly examined. The third method, while capable of truly predicting essentially any possible domain shape, is by no means the most efficient means of doing so.

Recently, we brought a fourth method to the prediction of domain shapes: a numerical solution of the differential

equation formed by setting the first functional derivative of energy (with respect to shape) equal to zero [18,19]. Through the remainder of this paper, we shall refer to this method as the direct, or numerical, calculation. Three key results came from this study. First, only two classes of domain shapes are stable. When the ratio ( $\Gamma$ ) of dipolar repulsion to interfacial tension is small, circles are the only stable domain shape. When this ratio is large, the only stable domain shapes are bilobes—the domain is elongated in a single direction, usually with slightly swollen ends. Second, both circles and bilobes are stable for a measurable (albeit small) range of  $\Gamma$ . Because of this, the transition from circles to bilobes is discontinuous. Third, as bilobed domains become increasingly elongated, the energy profile flattens; i.e., the second functional derivative with respect to shape decays rapidly to zero in the neighborhood of energy minimizing shapes. This limits the range of applicability of the numerical solution. As the numerical roundoff error overshadows the true value of the second derivative, this method becomes nonconvergent.

In this paper, we expand upon our previous work by introducing a metropolis Monte Carlo simulation for the prediction of domain shapes. None of the four shape prediction methods listed above examines the effect of entropy on domain shape; thus their results truly apply only in the limit as temperature approaches absolute zero. Metropolis Monte Carlo, on the other hand, explicitly incorporates temperature as a simulation parameter. The effect of temperature—and thus entropy—on domain shape can therefore be examined. Furthermore, the flat energy profile which comes with increased elongation does not limit the ability to execute the simulation. It simply allows for larger shape fluctuations. We should note that this is not the first study to use Metropolis Monte Carlo to simulate domain shape. Hurley and Singer [20,21] used simulation to examine the so-called “bubble to stripe transition” using a hexagonal Ising lattice. That particular study, however, focused primarily on the size and spatial arrangement of domains rather than the detailed shapes of individual domains.

\*Author to whom correspondence should be addressed.

Section II presents the details of our simulation method. Specifically, it examines the energy functional (or Hamiltonian), the computational evaluation of the Hamiltonian, the computational (i.e., discretized) representation of domain shape, our algorithm to generate Monte Carlo steps, and the metrics used to report shape. Section III uses this simulation technique to explore how the key physical parameters effect domain shape. In addition, by examining how simulation procedure affects domain shape, some conclusions are drawn as to how the experimental procedure may affect domain shape in the physical system.

## II. METHOD

The three key components of any Metropolis Monte Carlo simulation are the Hamiltonian, the computational representation of the physical system, and the algorithm used to generate the random changes. This section details how we apply these components in our simulation and presents the scalar metrics we use to report domain shape.

### A. Hamiltonian

Following the analysis of Keller, Korb, and McConnell [11], two shape dependent contributions to the energy of an isolated dipolar domain are identified. The first, line tension, scales with the perimeter of the domain, the length of the interface between the low and high density phases. This contribution attempts to minimize perimeter, thus promoting compact domains. The second, dipolar repulsion, scales with the sum of the cube of reciprocal distance between the individual pairs of dipoles which comprise the domain; the dipoles are assumed perpendicular to the plane of the system. This contribution attempts to increase the distance between dipoles, thus promoting elongated domains. Combined, these two opposing contributions produce the Hamiltonian

$$\mathcal{H} = \lambda P + \frac{\mu^2}{2} \int \int_D d^2\mathbf{r} \int \int_D \frac{h(|\mathbf{r} - \mathbf{r}'| - \delta)}{|\mathbf{r} - \mathbf{r}'|^3} d^2\mathbf{r}'. \quad (2.1)$$

Here  $\lambda$ ,  $P$ , and  $\mu$  represent, respectively, the line tension, the domain perimeter, and the excess dipole density of the domain relative to the surrounding phase. The integration limit  $D$  in the electrostatic integral represents all points in the domain—covering an area  $\mathcal{A}$ . The function  $h(x)$ , the Heaviside function, is defined to equal one if  $x$  is positive and zero otherwise. Mathematically, its presence in Eq. (2.1) prevents the inclusion of a nonintegrable singularity. Physically, it represents the pair distribution of dipoles in its simplest form: individual dipoles do not overlap and their distribution becomes uncorrelated for large separation. The parameter  $\delta$  is on the scale of the nearest neighbor dipole separation.

To generalize the simulation results, it is useful to rewrite the Hamiltonian in dimensionless form. Scaling all lengths by  $\delta$ , all areas by  $\delta^2$ , and all energies by  $kT$  yields

$$\hat{\mathcal{H}} = \frac{\hat{P}}{\Theta} + \frac{\Gamma}{2\Theta} \int \int_{\hat{D}} d^2\mathbf{r} \int \int_{\hat{D}} \frac{h(|\mathbf{r} - \mathbf{r}'| - 1)}{|\mathbf{r} - \mathbf{r}'|^3} d^2\mathbf{r}', \quad (2.2)$$

where  $\hat{\mathcal{H}} = \mathcal{H}/kT$ ,  $\hat{P} = P/\delta$ ,  $\Theta = kT/\lambda\delta$ , and  $\Gamma = \mu^2/\lambda$ . The integration limit  $\hat{D}$  represents all points in the domain—

covering a dimensionless area  $\hat{\mathcal{A}} (= \mathcal{A}/\delta^2)$ . For typographic simplicity, the hats will henceforth be dropped, but all references to  $\mathcal{H}$ ,  $P$ , and  $\mathcal{A}$  should be assumed dimensionless. From Eq. (2.2), it is clear that the Hamiltonian is a function of three parameters: the ratio of electrostatic to interfacial contributions ( $\Gamma$ ), the dimensionless temperature ( $\Theta$ ), and domain area ( $\mathcal{A}$ ).

As is common with Monte Carlo simulations, the computational bottleneck lies in the evaluation of the Hamiltonian; for our particular simulation it lies in the electrostatic integral. Any amount of analytic evaluation of the energy functional which can be performed reduces the required degree of numerical integration and thus is highly desirable. Through two judiciously selected coordinate transformations—outlined in Appendix A—the electrostatic term of Eq. (2.2) can be reduced from a double area integral (four dimensions) to a double contour integral (two dimensions). Specifically

$$\mathcal{H} = \frac{P}{\Theta} + \frac{\pi\mathcal{A}\Gamma}{\Theta} - \frac{\Gamma}{2\Theta} \oint ds \oint \frac{\Psi(s, s')}{\rho(s, s')} (\mathbf{e}_\rho \times \mathbf{e}_s) \cdot (\mathbf{e}_{s'} \times \mathbf{e}_\rho) ds', \quad (2.3)$$

where

$$\Psi(s, s') = \begin{cases} 1 + \ln \rho(s, s') & \text{if } \rho(s, s') > 1 \\ \rho(s, s') & \text{if } \rho(s, s') \leq 1 \end{cases}. \quad (2.4)$$

The integration variables  $s$  and  $s'$  represent the arclength along the perimeter of the domain from an arbitrary point on the perimeter, the unit vectors  $\mathbf{e}_s$  and  $\mathbf{e}_{s'}$  represent the tangents to the domain perimeter at points  $s$  and  $s'$ , the function  $\rho(s, s')$  represents the length of the line segment connecting point  $s$  to point  $s'$ , and the unit vector  $\mathbf{e}_\rho$  points in the direction from  $s$  to  $s'$ .

### B. Simulation method

The selection of the computational representation of domain shapes was driven by two criteria: flexibility and efficiency. With the goal of simulating the shape of a domain, the representation should be capable of portraying a wide spectrum of shapes with minimal restrictions. Furthermore, it should lend itself to computational efficiency, both in the evaluation of the Hamiltonian and in the generation of the random moves (perturbations). The literature is rich with examples of two dimensional shape simulations, mostly in the context of vesicles [22–29] and cyclic chains [30–32]. Although the contributions to the Hamiltonians governing these simulations—pressure differences between interior and exterior [23–28], chain rigidity [23–29], composition along the perimeter [27], and external potential fields [28–30]—are fundamentally different than those for the dipolar domain, these simulations do serve as templates for our simulation.

Borrowing from those simulations [24, 25, 28, 30, 31] which use a ‘‘pearl necklace’’ approach, we similarly represent the domain shape with an  $N$ -sided simple closed polygon. The number of sides may vary between simulations, but remains constant within any given simulation. The vertices of the polygon are not restricted to any grid or lattice. They may be located anywhere in the plane provided that the polygon does not intersect itself and that its area remains  $\mathcal{A}$ . Admittedly,

this polygon representation is not the most sophisticated shape model available to us. The Fourier expansion, for example, described by Ostrowsky and Peyraud [23] to generate a simple closed curve, for example, has been used in many vesicle simulations [26,27,29]. But with additional sophistication comes additional complexity. Polygons are quite capable of capturing all but the finest detail of domain shape while maintaining computational simplicity.

The polygon representation of domain shape brings with it two highly attractive computational advantages. First, its simplicity immediately leads to less computational overhead. Generation of Monte Carlo moves requires no more than the selection of a set of vertices to move and a set of new positions to which to move them. Compared to the iterative closure [23] required for each perturbation of the Fourier expansion of domain shape, the CPU time required to generate these moves is inconsequential. The second computational advantage, while not instantly obvious, is more significant. By considering the polygon as a collection of line segments, the Hamiltonian can be completely integrated analytically—as detailed in Appendix B. It is improbable that this is true for more sophisticated shape representations. The computational time necessary to numerically integrate the energy functional (given current resources) would certainly render this simulation either expensive or unfeasible, even with the analytic reduction of Eq. (2.2).

The algorithm used to generate Monte Carlo moves for our simulation must satisfy the condition that the area of the domain remains constant. This is fundamentally different from the “pearl necklace” representation used in the simulations cited above. In those simulations, the perimeter of the vesicle was held constant while area fluctuated. A new move generation algorithm is necessary. While many area preserving algorithms can easily be devised, they do not all satisfy the necessary condition of microscopic reversibility. Our method, which follows, satisfies both the area preservation and microscopic reversibility condition. Two vertices are chosen with even probability from all vertices of the polygon. Because both vertices are chosen from the set of all vertices, they may be separated by one or more vertices, they may be neighboring vertices, or they may be the same vertex. If they are separated by one or more vertices, the first vertex is displaced with even probability to a new position within radius  $R_m$  about its old position and the second vertex is displaced perpendicular to the line segment connecting its two neighboring vertices so as to restore the domain area; see Fig. 1(a). If the two vertices are neighbors, the first vertex is again displaced with even probability to a new position within radius  $R_m$  but the second vertex is displaced perpendicular to the line segment connecting the two vertices which neighbor the pair of randomly selected vertices; see Fig. 1(b). If the two vertices are in fact the same vertex, this vertex is displaced parallel to the line segment connecting its neighbors by a distance  $r$  chosen with probability  $P(r) = [\sqrt{R_m^2 - r^2} / (\pi/2)R_m^2]$ ; see Fig. 1(c). Note that this is fully equivalent to displacing the vertex within a circle of radius  $R_m$  followed by a displacement perpendicular to the line segment connecting its neighbors so as to preserve area. If any move causes the polygon to intersect itself, that move is immediately rejected.

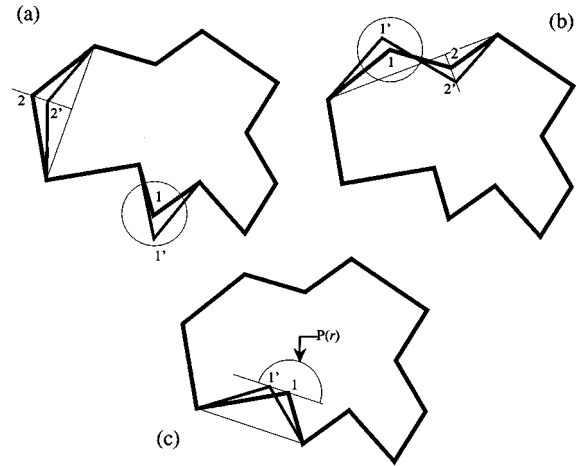


FIG. 1. Generation of Monte Carlo moves. Two vertices are selected at random. The first (1) is moved randomly to a new position ( $1'$ ) within radius  $R_m$  of its original position. The second (2) is moved deterministically to a new position ( $2'$ ) so as to maintain domain area and microscopic reversibility. Three possible scenarios exist: (a) the two vertices are separated by one or more vertices, (b) the two vertices are neighbors, or (c) the two vertices are actually the same vertex.

Because this move generation algorithm can (and will) result in a polygon with a large distribution of edge lengths, it is useful to include an additional term in the Hamiltonian which penalizes a large standard deviation in edge length

$$\mathcal{H}^\sigma = \chi \sum_i^N (p_i - \langle p \rangle)^2. \quad (2.5)$$

Here  $p_i$  represents the length of edge  $i$  and  $\langle p \rangle$  represents the average edge length. The value of  $\chi$  should be chosen such that  $\mathcal{H}^\sigma$  contributes only a very small fraction of the overall value of the Hamiltonian. For the simulation results reported in this paper,  $\chi=0.01$ , for which the maximum contribution of  $\mathcal{H}^\sigma$  to the overall Hamiltonian was found to be less than 0.01%. Note that this contribution does not penalize large domain perimeter, and therefore should not penalize either elongation or branching of the domain.

### C. Shape metrics

Because of the inherently graphical nature of the prediction of domain shapes, defining useful metrics to report results is essential. For the results which appear in this paper, domain shape is reported by perimeter and number of branches. In addition—because shape cannot be fully described by any finite set of scalars—representative snapshots, i.e., single Monte Carlo steps, of domain shape are provided to aid in the discussion of selected simulations [33].

The definition and interpretation of domain perimeter is entirely straightforward. It is computed by adding together the lengths of all of the edges of the polygon. Perimeter is minimized for circular domains—or in this case by regular  $N$ -gons. A small perimeter therefore indicates a compact domain shape. A large perimeter indicates either a long skinny domain or a domain which is highly branched—or forked—where each of the branches is thin on the scale of the overall

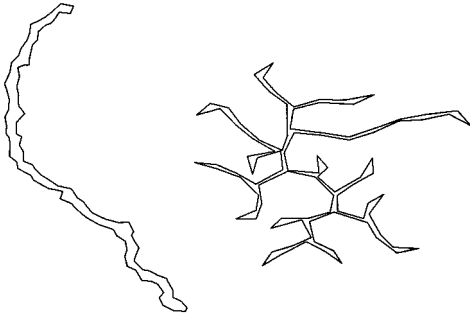


FIG. 2. Two elongated domains. Although the overall shape of the domain on the right appears roughly circular, it is composed of branches which individually are elongated.

domain shape. For domains with large perimeter, the width of the domain (or its branches) will be significantly smaller than the length (or lengths). The perimeter metric can therefore also serve as a surrogate measure of domain width, approximately  $2\mathcal{A}/P$ . We shall henceforth use the term “elongated” to refer to any large perimeter domain. In the case of highly branched domains, this elongation might be found only within individual branches; the overall domain shape, the ensemble of all branches, may appear roughly circular as in Fig. 2.

The definition and interpretation of the number of branches, on the other hand, is not so straightforward. For the results reported in this paper, the number of branches is determined using techniques borrowed from computational image analysis [34–36]. The domain is mapped onto a pixel grid; all pixels interior to the polygon are set to 1 and all pixels exterior to the polygon are set to 0. The resulting binarized image is skeletonized and the number of branches defined as the number of limbs in the skeleton—see Appendix C. This method of assigning a scalar to describe the character of a shape works both for compact and elongated domains. Its interpretation, however, differs slightly between these two cases. A compact domain exhibiting three branches, for example, appears roughly triangular while an elongated domain appears as three distinct branches joined by a triple point.

We must note at this point that the number of branches metric as reported in this paper should only be interpreted qualitatively. Quantitative interpretation is thwarted by a combination of finite size effect and current computational limitations. Increasing the number of edges in the polygon used to represent domain shape while holding all else constant, results in an increasing number of branches predicted by the simulation. For the values of  $N$  that we examined ( $N=100, 200, 500, 1000$ , and  $2000$ ), no indication of an approach to an asymptotic value was seen. Increasing  $N$  much above 2000 becomes computationally prohibitive as the time required for a simulation scales roughly as  $N^2$ .

As will be demonstrated in Sec. III, the qualitative information provided by the number of branches metric furnishes a useful complement to the perimeter metric in understanding the nature of domain shape transitions. Perimeter alone can only describe the elongation, and thus width, of a domain. It cannot describe the fundamental visual character of the shape. The number of branches metric helps to fill this void. Although, the exact magnitude of the number of

branches cannot be extracted from the results which follow, the observed trends in the number of branches show no indication of being finite size limited. The same trends were observed in all plots of a given simulation differing only in  $N$ . Moreover, by scaling only the number of branches axes, the plotted results from any set of simulations which differ only in  $N$  can be made to coincide.

### III. RESULTS AND DISCUSSION

The results which follow are grouped into five simulation experiments. The first three examine how domain shape is affected by the three simulation parameters:  $\Gamma$ ,  $\Theta$ , and  $\mathcal{A}$ . The next two examine how domain shape is affected by simulation procedure and from this extrapolate how domain shape may be affected by experimental procedure in a physical system. Specifically, they examine the effects of hysteresis and elongation rate. Finally, a short analysis about the prediction of domain shapes based on the results from these simulation experiments is presented.

Unless otherwise stated, all of the simulations reported below follow the same basic template. Domain area is  $100^2\pi$ . Domain shape is represented by a centagon ( $N=100$ ). The shape used to seed each simulation is defined by unique set of vertices  $(x_i, y_i)$  generated by the trigonometric expansion,

$$\frac{x_i}{\alpha} = \cos(\theta_i) + \sum_{j=1}^5 A_{x,j} \cos(j\theta_i) + B_{x,j} \sin(j\theta_i)$$

$$\frac{y_i}{\alpha} = \sin(\theta_i) + \sum_{j=1}^5 A_{y,j} \cos(j\theta_i) + B_{y,j} \sin(j\theta_i), \quad (3.1)$$

where the angle  $\theta_i = (2\pi i/N)$ , the coefficients  $(A_{x,j}, A_{y,j}, B_{x,j},$  and  $B_{y,j})$  are randomly assigned values between  $-0.2$  and  $0.2$ , and the scaling factor  $\alpha$  is chosen so that area equals  $\mathcal{A}$ . Each simulation is run for  $2000N$  successful Monte Carlo steps before any shape statistics are collected. Statistics on perimeter and number of branches are then collected until the simulation completes another  $20\,000N$  successful steps. The ratio of accepted to attempted moves is held between 40% and 60% by doubling or halving the move radius  $R_m$ , as necessary, after every 500 accepted moves.

#### A. Experiments 1–3: Variation of $\Gamma$ , $\Theta$ , and $\mathcal{A}$

The first parameter examined is  $\Gamma$ , the dimensionless ratio of electrostatic repulsion to interfacial tension. Figure 3 plots the mean domain shape—measured by perimeter and number of branches—as a function of  $\Gamma$  for  $\Theta=0.01$ . Inlaid shapes depict representative domain shapes from individual Monte Carlo steps. A clear transition in domain shape occurs in the neighborhood of  $\Gamma=0.21$ . Below this point, domains are fairly compact and the average number of branches is essentially zero. Above the transition, domains become increasingly elongated and exhibit a growing number of branches as  $\Gamma$  increases. The error bars shown in Fig. 3 represent the fluctuations—specifically the standard deviation—in the perimeter and number of branches, not an uncertainty in measurement. Interestingly, the fluctuations in perimeter are greatest in the neighborhood of the transition while fluctua-

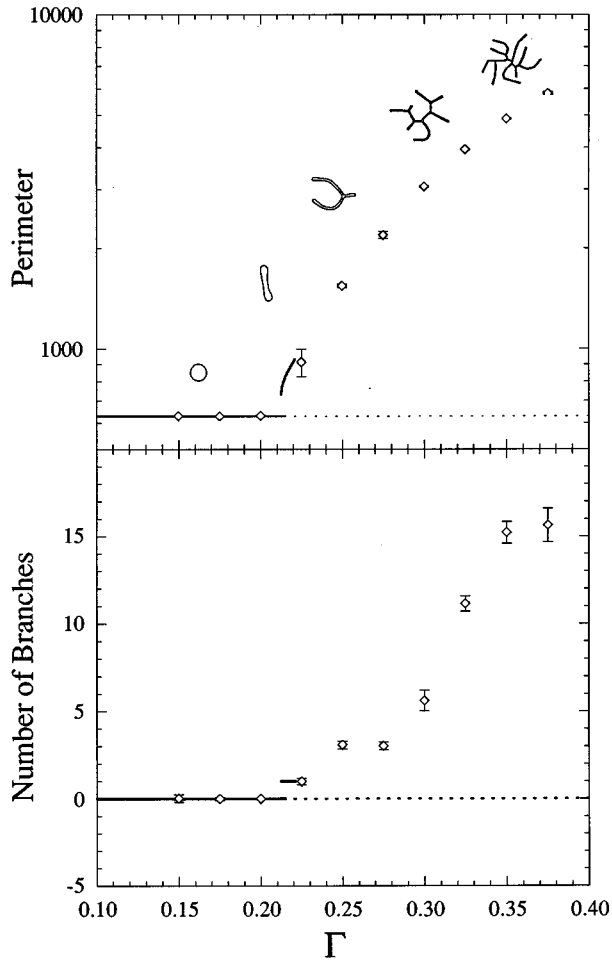


FIG. 3. Domain perimeter as a function of  $\Gamma$ . Each data point ( $\diamond$ ) represents the mean domain perimeter for an individual simulation. Error bars indicate standard deviation (fluctuation) of perimeter. All simulations were run at  $\Theta=0.01$  with  $\mathcal{A}=100^2\pi$  and  $N=100$ . Solid lines represents the perimeter of domain shapes calculated [18] to minimize the energy functional Eq. (2.1). The dotted line represents the perimeter of a circular domain. Inset figures show sample simulation steps.

tions in the number of branches grows with  $\Gamma$ . Finally, it is important to note that very little scatter is seen in the perimeter data, while the scatter in the number of branches is quite large—much larger than the fluctuations. This will be discussed further as more results are presented.

Figure 3 also demonstrates that the simulation agrees quite well with the direct calculation of energy minimizing shapes [18]. They agree on the value of  $\Gamma$  for which the transition from circular to elongated (i.e., large perimeter) domains occurs; the calculation predicts a transition  $\Gamma$  of 0.214. Although the direct calculation plot had to be truncated at  $\Gamma=0.221$  because of nonconvergence, both perimeter plots appear to follow the same curve above the elongation transition. The direct calculation predicted that the transition from circular to elongated domains is discontinuous, i.e., first order. Although too few simulation data points are shown to determine if the transition is discontinuous or continuous, the large fluctuation (in perimeter) for the simulation at  $\Gamma=0.225$  strongly suggests that the domain may be oscillating between two, or more, distinct energy minimizing

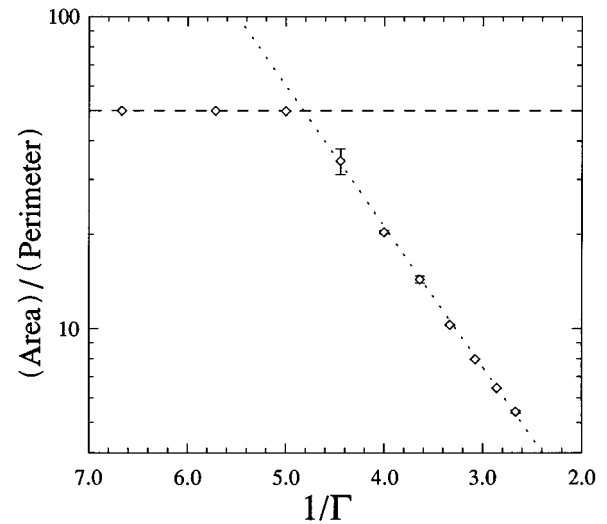


FIG. 4. Exponential growth of domain width with reciprocal  $\Gamma$ . Figure 3 is replotted as mean ratio of domain area to perimeter, which is approximately equal to half the width of the branches of elongated domains, on a log scale as a function of  $1/\Gamma$ . Error bars indicate fluctuation of  $A/P$  due to standard deviation (fluctuation) of perimeter. The dashed line represents circular domains. The dotted line shows a fit through the data equal to  $0.33 \exp(1.0/\Gamma)$ .

shapes. One obvious difference, however, exists between the simulation and the direct calculation results: the predicted number of branches. While calculation predicts only bilobed and circular domains, the simulation finds that domains become increasingly branched as  $\Gamma$  increases. The reason for this will be explained as further simulation results are covered.

The simulation results shown in Fig. 3 agree not only with our prior work, they follow a basic trend which has been observed repeatedly from the very start of domain shape calculations [12,20,37]. The characteristic length scale at which circular domains give way to more elongated shapes scales exponentially with the ratio of line tension to dipole strength (i.e.,  $\exp(1/\Gamma)$ ). We have chosen to show the transition from circular to elongated domains as a function of  $\Gamma$  for a fixed domain area rather than the transition as a function of area for a fixed  $\Gamma$ . In this context, the appropriate length scale to examine is the width of the domain (or domain branches). Figure 4 clearly shows that once the domain is no longer circular, its width (as approximated by the ratio of area to perimeter) scales exponentially with  $1/\Gamma$ .

The second parameter examined is  $\Theta$ , the dimensionless temperature; in particular, its effect on the transition from compact to elongated domains. Figure 5 plots domain shape—perimeter and number of branches—as a function of  $\Gamma$  for various  $\Theta$ . From the perimeter plot, it is immediately apparent that the onset of domain elongation occurs at increasingly smaller  $\Gamma$  with increasing temperature. Moreover, while a clear transition from compact to elongated domains can be seen in the neighborhood of  $\Gamma=0.21$  for  $\Theta<0.1$ , the elongation for  $\Theta>1$  is too gradual to identify a value or range of  $\Gamma$  with this transition. Interestingly, fluctuations in domain perimeter do not appear to necessarily increase with temperature; the largest fluctuations occur for low  $\Theta$  near the transition. Finally, the number of branches appears to be de-

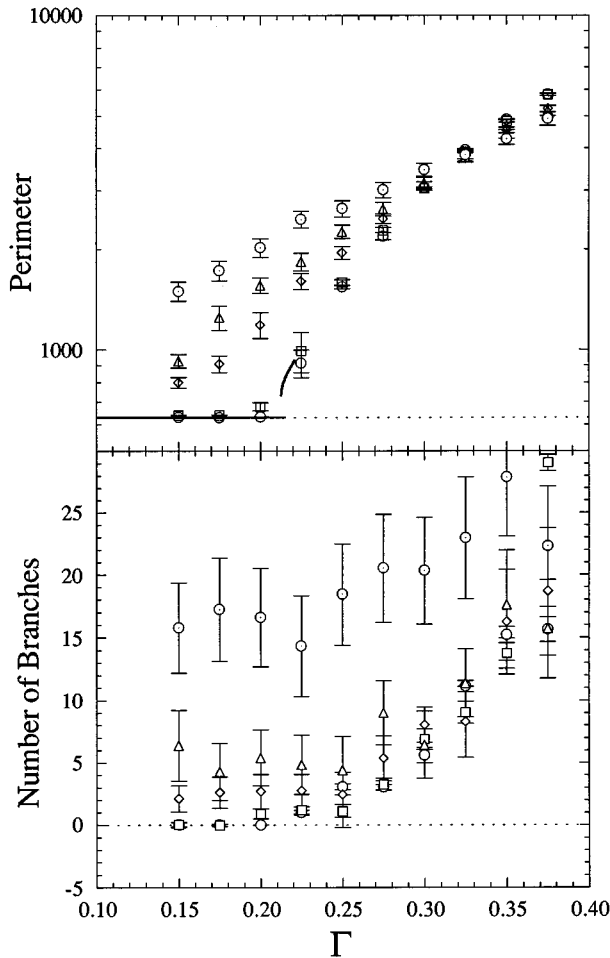


FIG. 5. Effect of temperature on domain shape. Mean perimeter and mean number of branches are plotted for  $\Theta=0.01$  ( $\circ$ ),  $\Theta=0.1$  ( $\square$ ),  $\Theta=1$  ( $\diamond$ ),  $\Theta=2$  ( $\triangle$ ), and  $\Theta=5$  ( $\odot$ ). All simulations were run with  $N=100$ . Error bars indicate standard deviations (fluctuation about mean).

terminated primarily by temperature for small  $\Gamma$  and primarily by  $\Gamma$  for large  $\Gamma$ . The fluctuation in the number of branches increases with temperature and appears to be relatively unaffected by  $\Gamma$ .

To demonstrate the effects that temperature has on the number of branches [33], Fig. 6 shows sequences from four of the simulations represented in Fig. 5. Domains at high  $\Theta$  are rougher than those at low  $\Theta$ ; they exhibit many more outcroppings, or jags. In addition, domains at high  $\Gamma$  exhibit more branches than those at low  $\Gamma$ . The skeletonization procedure used to compute number of branches counts both the true branches—the major topographic features—and any substantial outcroppings. Thus, for low  $\Gamma$ , when the number of outcroppings greatly exceeds the number of true branches, the reported number of branches reflects a strong dependence on  $\Theta$ . For high  $\Gamma$ , as the number of true branches increases, the reported number of branches becomes more strongly influenced by  $\Gamma$ . For both low and high  $\Gamma$ , the number of true branches remains fairly static throughout any simulation while the outcroppings are highly dynamic. The fluctuation in the reported number of branches therefore is influenced primarily by  $\Theta$ .

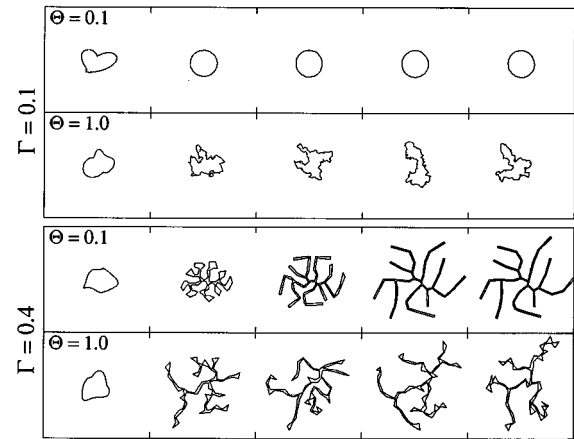


FIG. 6. Sample sequences from four simulations. The top two sequences are from simulations run at  $\Gamma=0.1$ ; the bottom sequences two at  $\Gamma=0.4$ . The first and third sequences are from simulations run at  $\Theta=0.1$ ; the second and third at  $\Theta=1$ . The first image in each sequence is the shape used to seed the simulation; the remaining four from steps evenly spaced through the course of the simulation.

Figure 7 shows the effect that temperature has on the exponential scaling of domain width. It would appear that this well established scaling applies fully, as with the discontinuous transition, only at the zero temperature limit. As the temperature increases, elongation begins at lower  $\Gamma$  and thus the domain width begins decreasing sooner, and does so in a nonexponential manner. The data shown in the figure do, however, suggest that the domain width will asymptotically approach the exponential decay as it moves deeper into the elongation region (larger  $\Gamma$ ).

The final parameter examined is  $\mathcal{A}$ , the dimensionless domain area. As domain size increases, the elongation transi-

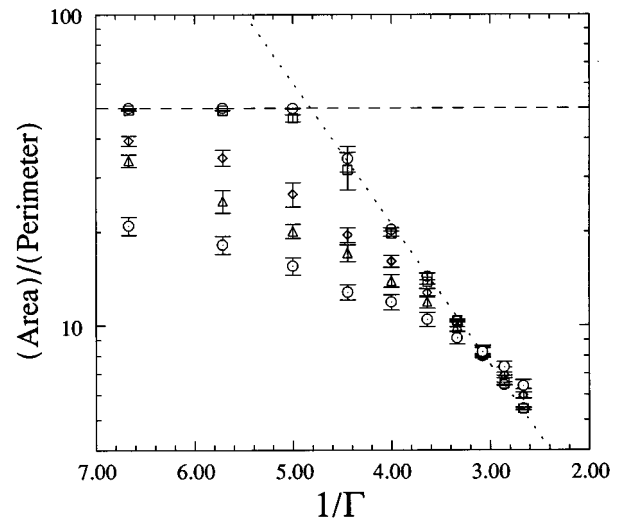


FIG. 7. Effect of temperature on the exponential growth of domain width with reciprocal  $\Gamma$ . Figure 5 is replotted as mean ratio of domain area to perimeter on a log scale as a function of  $1/\Gamma$  for  $\Theta=0.01$  ( $\circ$ ),  $\Theta=0.1$  ( $\square$ ),  $\Theta=1$  ( $\diamond$ ),  $\Theta=2$  ( $\triangle$ ), and  $\Theta=5$  ( $\odot$ ). Error bars indicate fluctuation of  $A/P$  due to standard deviation (fluctuation) of perimeter. The dashed line represents circular domains. The dotted line shows a fit through the data equal to  $0.33 \exp(1.0/\Gamma)$ .

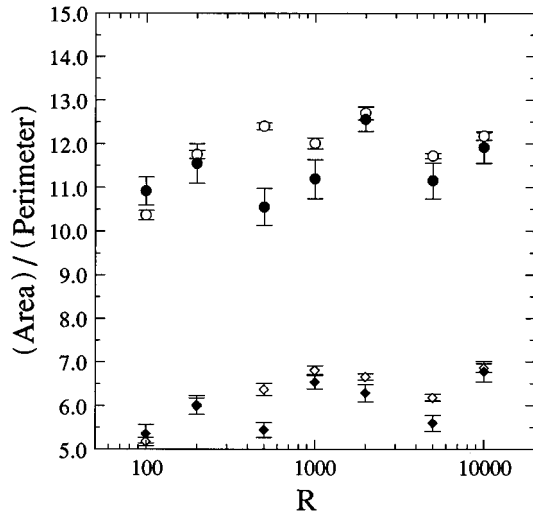


FIG. 8. Effect of domain area on the width of domain branches. Mean ratio of domain area to perimeter, which is approximately equal to half the width of the branches of elongated domains, is plotted as a function of equivalent domain radius ( $\sqrt{A/\pi}$ ). Results are shown for simulations run at two values of  $\Gamma$ , 0.3 (circles) and 0.4 (diamonds), and at two values of  $\Theta$ , 0.1 (open points) and 1 (filled points). All simulations are run with  $N=100$ .

tion shifts to increasingly lower  $\Gamma$ . This completely agrees with what has been found in numerous other studies which examined the effect of domain size on shape [5,6,12,14,18]. Aside from the shift in the transition to lower  $\Gamma$ , it is difficult to extract any useful information about how the domain area affects domain shape from plots of shape versus  $\Gamma$ . It is more interesting, however, to examine how the character of domain branches is affected by domain size. Figure 8 plots the ratio of the domain area to the perimeter as a function of domain size for two values of  $\Gamma$  and two values of  $\Theta$ . Both values of  $\Gamma$  (0.3 and 0.4) are chosen well above the elongation transition for all  $A$  shown. The ratio of area to perimeter can therefore be interpreted as a measure of the width of the branches. The width of the domain branches is clearly independent (or only weakly dependent) upon domain size; it is a function only of  $\Gamma$  and  $\Theta$ . Larger domains must therefore exhibit either longer branches or more branches (or some combination thereof) than smaller domains at the same  $\Gamma$  and  $\Theta$ .

### B. Experiments 4–5: Variation of simulation procedure

As suggested by the sequences shown in Fig. 6, and as clearly visible when viewing animated sequences from sample simulations [33], the number and configuration of the true branches remain fairly static throughout a simulation once they have been established. These aspects of domain shape are therefore highly dependent upon the initial (or seed) shape. This, presumably, is the source of the notable scatter in the number of branches plotted in Fig. 3. Because of this dependence on the initial formation of branches, each simulation samples only a small subset of the large set of energetically accessible domain shapes. This has two immediate implications on how the results from simulations of

domain shape are interpreted. The first is that care should be taken before treating the simulation results as thermodynamic properties. The second implication is that it should be possible to design simulation experiments which mimic certain aspects of physical experiments. The two simulation experiments which follow take advantage of the latter implication to investigate shape hysteresis and the influence of elongation rate.

One of the key results found in the direct calculation of domain shape is that the transition from circular to bilobed domains is discontinuous. The shape should therefore exhibit hysteresis when the value of  $\Gamma$  is cycled through the transition. To simulate this behavior, a string of linked simulations is performed. The first simulation is seeded with a random shape and run with  $\Gamma=0.2$ . Subsequent simulations are seeded with the final shape of the preceding simulation and run with a value of  $\Gamma$  0.0025 greater than in the preceding. Once the value of  $\Gamma$  reaches 0.25, the process is reversed and  $\Gamma$  is decreased between each simulation in steps of 0.0025 until it is again 0.2. Figures 9, 10, and 11 show the results for these simulations for  $\Theta=0.01$ ,  $\Theta=0.1$ , and  $\Theta=1.0$ , respectively. At very low temperature ( $\Theta=0.01$ ), hysteresis is clearly observed in both perimeter and number of segments, which, except for near the ends of the loop, is either clearly 0 (roughly circular domains) or 1 (single branched domains). At low temperature ( $\Theta=0.1$ ), hysteresis is still observable, but signs of its disintegration are showing. The width is narrower and more importantly, the number of branches is showing mixtures of compact and elongated domains (values between 0 and 1). At high temperature ( $\Theta=1.0$ ), no sign of hysteresis remains. This is, of course, consistent with the finding that the well defined transition disappears with increasing  $\Theta$ . The number of branches, however, remains roughly constant with a value of 1.5, which can be seen from Fig. 5 to be the number of branches for a simulation with a random seed run at  $\Gamma=0.2$  and  $\Theta=1.0$ .

Comparison of the hysteresis results with Fig. 3 reveals an interesting discrepancy. In the low temperature hysteresis experiments, domains above the elongation transition exhibit only single branches; the number of branches shows no sign of increasing with increasing  $\Gamma$ . The core difference between the simulations run for Fig. 3 and the simulations run to examine hysteresis is in how they are seeded. In the hysteresis experiment, the domains are stepped slowly through the elongation transition. In the generation of Fig. 3, the domains are essentially plunged through the elongation transition in one quick step; because the seed shape is compact, it can be associated with low  $\Gamma$ . The rate of elongation apparently has a profound effect on domain shape. In a physical experiment, elongation can be induced either by adjusting  $\Gamma$  or by changing domain size, which shifts the transition  $\Gamma$ . The rate of elongation is controlled therefore by how fast  $\Gamma$  is changed or, more applicably, by how rapidly domains grow.

The final simulation experiment examines the effect that the rate of elongation has on domain shape by stringing together simulation sets as in the hysteresis experiment. The first simulation in each set uses a random seed and is run with  $\Gamma=0.2$ , well below the elongation transition. The last simulation in each set is run with  $\Gamma=0.4$ , well above the elongation transition. Within each set, the final shape of each simulation is used as the seed for the subsequent simulation

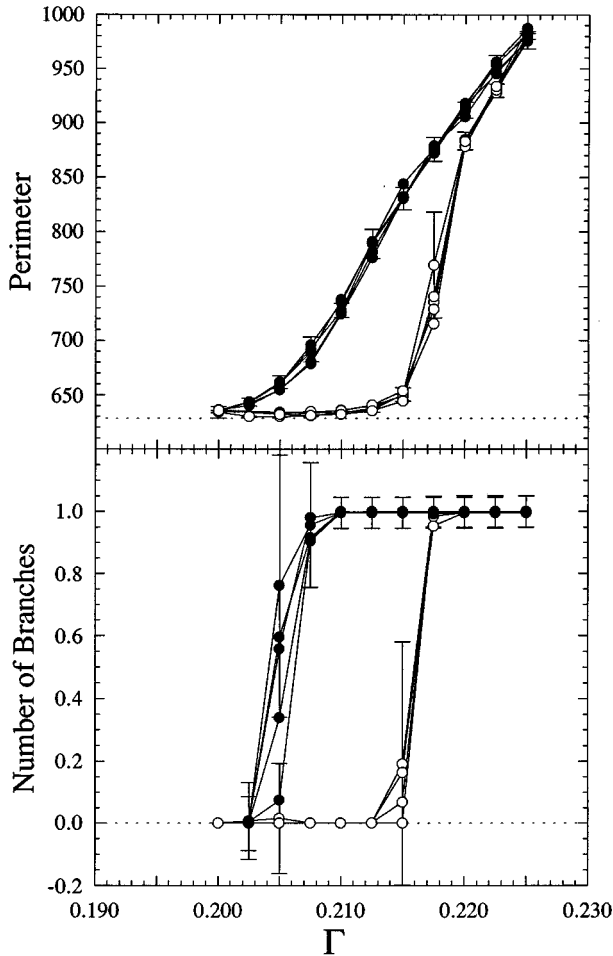


FIG. 9. Shape hysteresis near the elongation transition. Mean perimeter and number of branches are plotted for simulation sets run between  $\Gamma=0.2$  and  $\Gamma=0.4$ . Each simulation in the set (with the exception of the first) was seeded with the final step of the previous simulation. Data points representing increasing  $\Gamma$  are shown as open circles; data points for decreasing  $\Gamma$  as filled circles. Five increasing sequences and five decreasing sequences are shown; points within the same sequence are connected with tie lines. The dashed lines at  $P=628.3$  represents the minimum possible perimeter, i.e., a circular domain. All simulations were run at  $\Theta=0.01$  with  $N=100$ .

and the value of  $\Gamma$  is incremented by  $\Delta\Gamma$  between simulations. Small  $\Delta\Gamma$  corresponds to a slow progression through the transition. Large  $\Delta\Gamma$  corresponds to a rapid progression through the transition. Figure 12 shows the results for  $\Theta=0.1$  using  $\Delta\Gamma$  with values of 0.2, 0.1, 0.04, and 0.02. Figure 13 shows the same for  $\Theta=1.0$ . To demonstrate the effect visually, Fig. 14 shows one representative domain shape from each simulation at  $\Theta=1.0$ . At both high and low temperature, the number of branches clearly decreases with decreasing  $\Delta\Gamma$ . For  $\Delta\Gamma=0.02$ , nearly a magnitude larger than in the hysteresis experiment, domains exhibit only a single branch well into the elongation regime. This is especially interesting for  $\Theta=1.0$  since the domain shows a larger number of branches below the elongation transition. With increasing  $\Gamma$ , one of the branches ultimately dominates and the domain evolves into a single meandering branch.

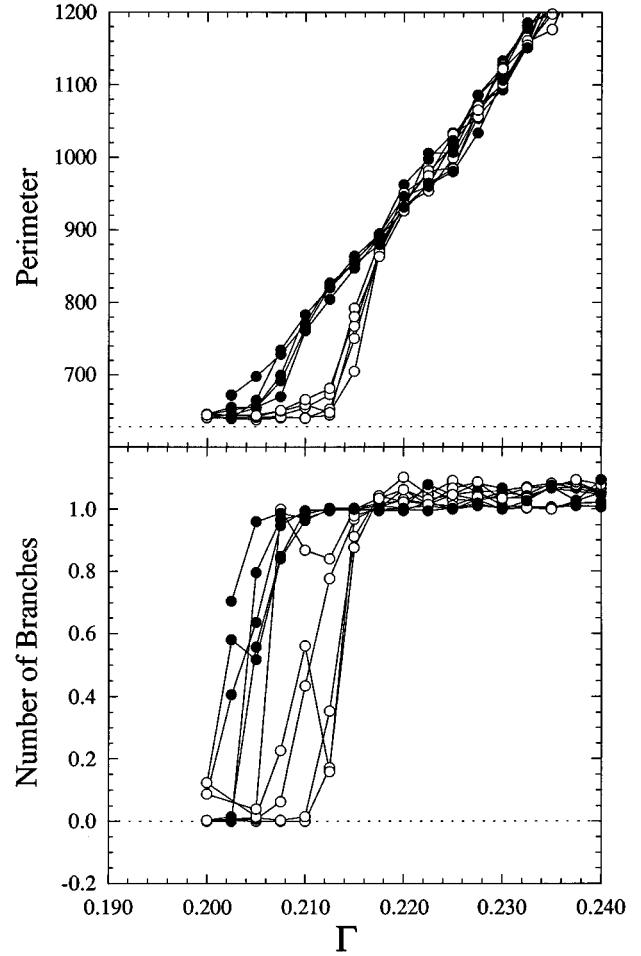


FIG. 10. Onset of loss of hysteresis near the elongation transition. Data is plotted exactly as for Fig. 9, except that simulations were run at  $\Theta=0.1$ .

### C. Analysis of experiments 1–5: Single vs multiple branched domains

The direct calculation predicts bilobed domains. The simulation predicts either single or multiple branched domains depending upon the rate of elongation. Table I lists the mean value of the Hamiltonian from various simulations which predict a different number of branches, in particular, those shown for  $\Gamma=0.4$  in Figs. 12–14. Clearly domains with fewer branches represent a lower energy level than those with many branches, but only marginally. Single branched domains remain the most energetically favored shape, but the driving force for a domain with multiple branches to become a single branch is negligibly weak. Similarly, for a single branch domain, the energy difference between a straight branch (or bilobe) and one which meanders is too small to detect. Both of these results are consistent with the direct calculation results, which predict that bilobed domains minimize an energy functional which is effectively flat in the neighborhood of this minimum.

The utility of any theoretical calculation or any simulation is in how it models the physical system. Figure 15 depicts an experimentally obtained fluorescence microscopy image of one phospholipid monolayer [38]. Although the domains of the simulation exist in isolation and those in the microscopy

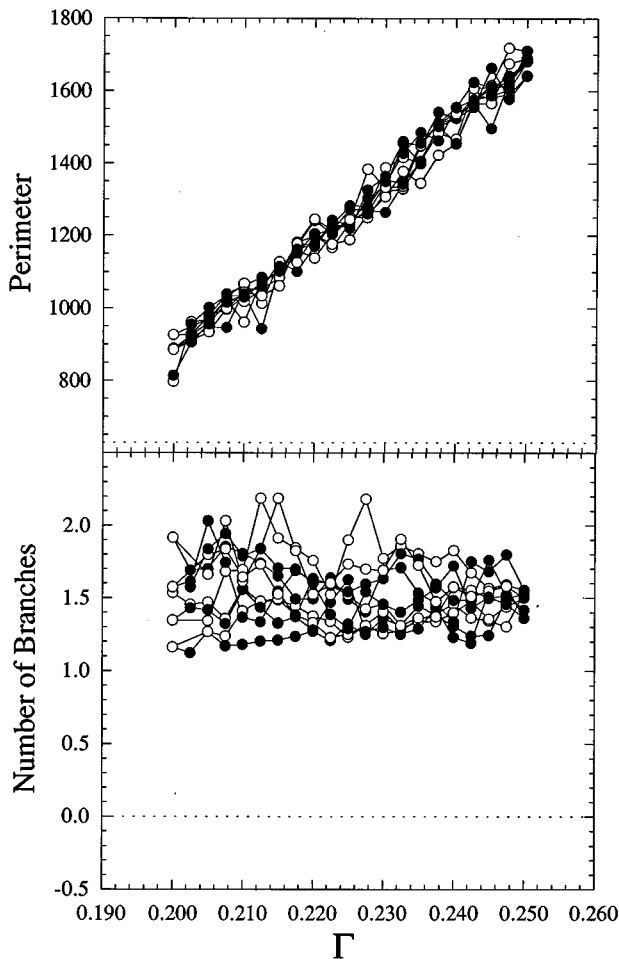


FIG. 11. Loss of hysteresis near the elongation transition. Data is plotted exactly as for Figs. 9 and 10, except that simulations were run at  $\Theta=1$ .

image have neighbors, the domains shown in the image demonstrate many of the characteristics predicted by simulation. First and foremost, they strongly resemble the shapes found in the simulations. All of the branches from all of the domains appear to be of roughly the same width. The larger domains tend to have more branches than smaller domains. These domains reside deeper within the elongation regime, and probably experienced a faster growth (thus elongation) rate. Both of these factors are predicted by the simulation to increase the observed number of branches.

The domain area used in the simulations reported above ( $100^2 \pi \delta^2$ ) was chosen to allow comparison of the simulation results to those of prior calculations. For room temperature (300 K), using a value of  $\lambda$  on the order of  $10^{-12} N$  [39], and a value of  $\delta$  on the order of  $10 \text{ \AA}$  (corresponding to a molecular area on the order of  $80 \text{ \AA}^2$ ), the value of the dimensionless temperature is roughly 4. This is clearly in the high temperature regime. The domains examined in typical phospholipid systems, however, are much larger than those examined in these simulations. Simulation domains have an area on the order of  $3 \times 10^{-6} \mu\text{m}^2$  (radii of 1 nm). Physical domains have an area on the order of  $2000 \mu\text{m}^2$  (radii of 25  $\mu\text{m}$ ). It can be argued both heuristically and empirically that the boundary between the low and high temperature regimes

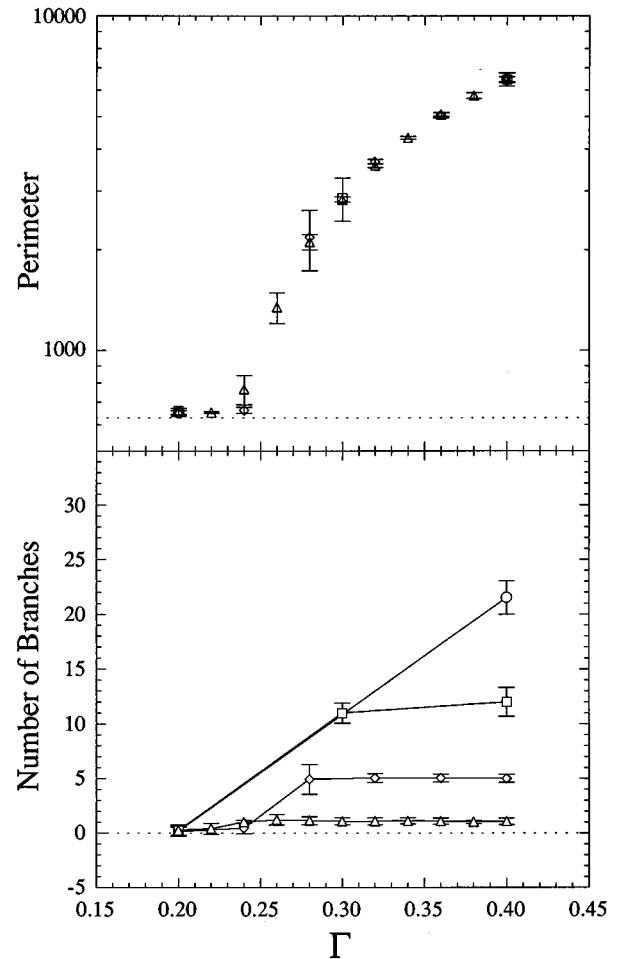


FIG. 12. Sensitivity of domain shape to rate of elongation. Mean perimeter and number of branches are plotted for simulation sets run from  $\Gamma=0.2$  to  $\Gamma=0.4$ . Each simulation in the set (with the exception of the first) was seeded with the final step of the previous simulation. The results shown are for sets making steps in  $\Gamma$  of 0.2 ( $\circ$ ), 0.1 ( $\square$ ), 0.04 ( $\diamond$ ), and 0.02 ( $\triangle$ ). All simulations were run at  $\Theta=0.1$  with  $N=100$ .

should increase with increasing domain size. Heuristically, larger domains should require larger shape fluctuations to induce a transition. Empirically, the definition of dimensionless temperature can be rewritten on the basis of domain size rather than on the basis of intermolecular distances (i.e.,  $\Theta' = [kT/\lambda R]$ ). The simulation then predicts a low temperature limit of  $\Theta' < 0.001$  and a high temperature limit of  $\Theta' > 0.01$ . For domains observed in the physical system,  $\Theta'$  is on the order of 0.0001, which is clearly now in the low temperature regime.

#### IV. CONCLUSIONS

Monte Carlo simulation can be a useful complement to direct calculation in the prediction of the shapes of domains observed in dipolar films. Using the polygon representation of domain shape presented in this paper, these simulations can be accomplished without sacrificing either generality or computational efficiency. The perimeter metric appears to be a fairly robust measure of domain shape, showing little to no dependence on any of the simulation particulars such as de-

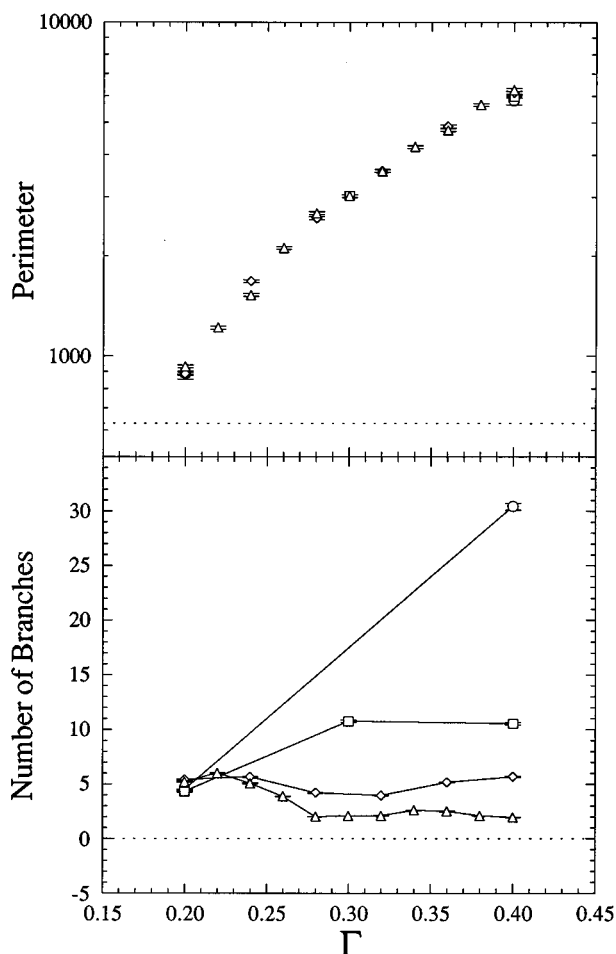


FIG. 13. Sensitivity of domain shape to rate of elongation. Data is plotted exactly as for Fig. 12, except with  $\Theta=1$ .

degree of discretization, seed shape, or even elongation rate. Nothing indicates that it cannot safely be interpreted as a thermodynamic property. The number of branches, on the other hand, is highly dependent upon many simulation particulars. The information it brings should be regarded quali-

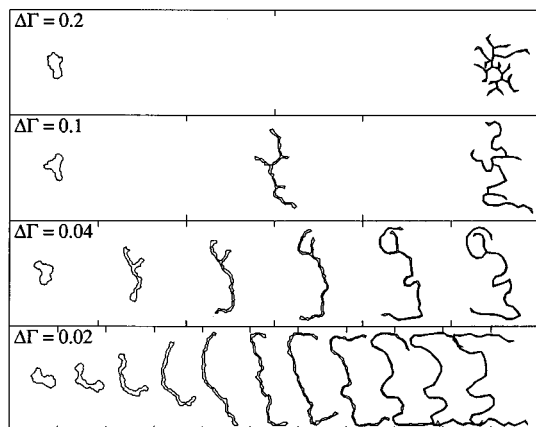


FIG. 14. Sample simulation steps from the simulation sets shown in Fig. 13. The first image in each sequence is from the simulation run at  $\Gamma=0.2$ ; the last from the simulation run at  $\Gamma=0.4$ . All simulations were run at  $\Theta=1$  with  $N=100$ .

TABLE I. Comparison of the Hamiltonian for domain shapes with a different number of branches. The values shown are from the simulations shown in Figs. 12–14 with  $\Gamma=0.4$ . Smaller  $\Delta\Gamma$  corresponds to fewer domain branches.

$\Theta$	$\Delta\Gamma$	Number of branches	Average Hamiltonian	St. dev. Hamiltonian
0.1	0.20	21.5	-2651.1	43.7
0.1	0.10	12.0	-2700.3	16.0
0.1	0.04	5.0	-2761.5	10.5
0.1	0.02	1.1	-2778.4	3.7
1.0	0.20	30.4	-2436.2	34.5
1.0	0.10	10.5	-2595.6	29.0
1.0	0.04	5.7	-2661.5	12.2
1.0	0.02	1.8	-2699.5	8.3

tatively rather than quantitatively. The qualitative information which it brings, however, provides insight into the visual nature of domain shape transitions. In addition, this dependence upon the simulation parameters allows for construction of simulation experiments which mimic aspects of physical experiments.

Simulation can provide information about domain shape unobtainable by calculation alone. In addition to many minor results, the simulation experiments reported herein yield four key results. The width of domain branches is a function of only  $\Gamma$  and  $\Theta$  and is independent of the size of the domain. The transition from compact to elongated domains, already known to be discontinuous in the zero temperature limit, is so only at low temperature; at high temperature, the elongation becomes continuous. Elongated domains may appear either as a single branch or with many branches depending upon the rate of elongation. While the conformation and roughness of individual branches may be fairly dynamic, the number of branches is reasonably static once established.

The simulation experiments presented in this paper represent only a fraction of the possibilities. Immediate examples include simulations seeded with elongated shapes rather than compact ones, experiments which treat area or temperature, rather than  $\Gamma$ , as the principle simulation parameter, and a thorough mapping of parameter space. Other examples might

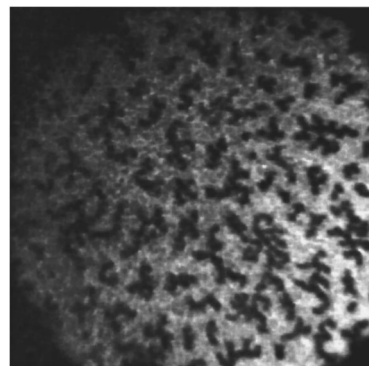


FIG. 15. Fluorescence microscopy image of an insoluble monolayer of a mixture of 50% *L*- $\alpha$ -dipalmitoyl-2-sn-glycero-phosphocholine (DPPC) and 50% 1-behenoyl-2-hydroxy-sn-glycero-phosphocholine at an air-water interface. Surface pressure is 13 dyne/cm. Area per lipid molecule is  $58.0 \text{ \AA}^2$ . Domains exhibit shapes similar to those seen in the simulation. Scale:  $1 \text{ cm} \approx 60 \text{ \mu m}$ .

include augmentation of the Hamiltonian to examine the effects of tilted dipoles or anisotropic line tension. Even more elaborate examples may require adaptation of the simulation technique such as to examine interactions between neighboring domains or the influence of confinement on the domains.

### ACKNOWLEDGMENTS

We gratefully acknowledge support for this work provided by the David and Lucile Packard Foundation and by the National Science Foundation (CTS-89-57051). In addition, M.A.M. wishes to express gratitude for financial support from Procter and Gamble.

### APPENDIX A

This appendix details the analytic reduction of the double area integral of the Hamiltonian to a double contour integral. Beginning with the expression for the electrostatic term as found in Eq. (2.2), the integral over  $d^2\mathbf{r}'$  is expanded using polar coordinates with the origin located at  $\mathbf{r}$ ,

$$\frac{H^\mu}{\Gamma/2\Theta} = \int \int_D d^2\mathbf{r} \int_0^{2\pi} \int_0^{\xi(\phi;\mathbf{r})} \frac{h(\eta-1)}{\eta^3} \eta d\eta d\phi. \quad (\text{A1})$$

Here, the coordinates  $\eta$  and  $\phi$  represent, respectively, the distance from  $\mathbf{r}$  and the polar angle. The upper limit of integration over  $\eta$ —the function  $\xi(\phi;\mathbf{r})$ —represents the distance from  $\mathbf{r}$  to the domain perimeter at angle  $\phi$ . Although  $\xi$  may be multivalued for some  $\phi$ , this does not hinder analytic evaluation.

The Heaviside function is moved out of the innermost integral by adjusting its argument and the lower limit of integration

$$\frac{H^\mu}{\Gamma/2\Theta} = \int \int_D d^2\mathbf{r} \int_0^{2\pi} h(\xi(\phi;\mathbf{r})-1) \int_1^{\xi(\phi;\mathbf{r})} \frac{d\eta}{\eta^2} d\phi. \quad (\text{A2})$$

The integral over  $\eta$  is evaluated analytically

$$\frac{H^\mu}{\Gamma/2\Theta} = \int \int_D d^2\mathbf{r} \int_0^{2\pi} h(\xi(\phi;\mathbf{r})-1) \frac{h(\xi(\phi;\mathbf{r})-1)}{\xi(\phi;\mathbf{r})} d\phi. \quad (\text{A3})$$

The identity  $h(x) = 1 - h(-x)$  is applied to the first term of the integrand

$$\begin{aligned} \frac{H^\mu}{\Gamma/2\Theta} &= \int \int_D d^2\mathbf{r} \int_0^{2\pi} 1 - h(1 - \xi(\phi;\mathbf{r})) \\ &\quad - \frac{h(\xi(\phi;\mathbf{r})-1)}{\xi(\phi;\mathbf{r})} d\phi, \end{aligned} \quad (\text{A4})$$

which can then be rewritten as,

$$\begin{aligned} \frac{H^\mu}{\Gamma/2\Theta} &= 2\pi A - \int \int_D d^2\mathbf{r} \int_0^{2\pi} \frac{d\phi}{\xi^*(\phi;\mathbf{r})} \\ &\quad \text{where } \xi^*(\phi;\mathbf{r}) = \max(\xi(\phi;\mathbf{r}), 1). \end{aligned} \quad (\text{A5})$$

Evaluation of the integral over  $d^2\mathbf{r}$  begins with reversal of the order of integration in Eq. (A5)

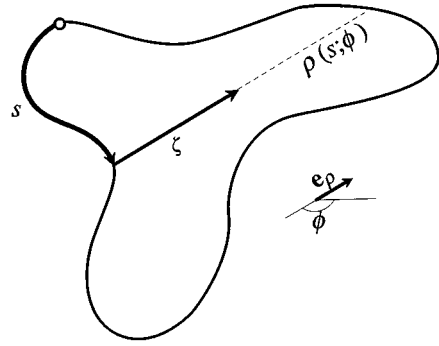


FIG. 16. Coordinate system used to evaluate Eq. (A7). The coordinate  $s$  represents distance along domain perimeter. The coordinate  $\zeta$  represents distance from point  $s$  at angle  $\pi + \phi$ , the direction of  $\mathbf{e}_\rho$ . Also shown here,  $\rho(s;\phi)$  represents the value(s) of  $\zeta$  for which  $(s,\zeta)$  is a point on the perimeter of the domain.

$$\frac{H^\mu}{\Gamma/2\Theta} = 2\pi A - \int_0^{2\pi} d\phi \int \int_D \frac{d^2\mathbf{r}}{\xi^*(\mathbf{r};\phi)}. \quad (\text{A6})$$

Note that  $\phi$  is now the integration variable for the outer integral and thus essentially a parameter to the inner integral. The inner integration is next expanded using a coordinate system designed specifically to allow further analytic evaluation. The coordinate  $s$  is defined as the arclength along the perimeter of the domain from an arbitrary fixed point on the perimeter. The unit vector  $\mathbf{e}_\rho$  is defined to point along the direction  $\pi + \phi$ . The coordinate  $\zeta$  is defined as the distance from point  $s$  on the perimeter in the direction of  $\mathbf{e}_\rho$  (see Fig. 16). Applying this coordinate system to Eq. (A6) yields

$$\frac{H^\mu}{\Gamma/2\Theta} = 2\pi A - \int_0^{2\pi} d\phi \oint ds |\mathbf{e}_s \times \mathbf{e}_\rho| \int_0^{\rho(s;\phi)} \frac{d\zeta}{\xi^*(\mathbf{r};\phi)}. \quad (\text{A7})$$

The upper limit of integration over  $d\zeta$ —the function  $\rho(s;\phi)$ —represents the distance from point  $s$  to the perimeter in the direction of  $\mathbf{e}_\rho$ . As with  $\xi(\phi;\mathbf{r})$ ,  $\rho(s;\phi)$  may be multiply defined for some values of  $s$  but will pose no problem.

The rationale behind this rather unique coordinate system can now be utilized. The coordinate  $\zeta$  and the function  $\xi(\mathbf{r};\phi)$ , although defined from opposite viewpoints, are geometrically identical. Substituting this identity into Eq. (A7) yields

$$\frac{H^\mu}{\Gamma/2\Theta} = 2\pi A - \int_0^{2\pi} d\phi \oint ds |\mathbf{e}_s \times \mathbf{e}_\rho| \int_0^{\rho(s;\phi)} \frac{d\zeta}{\max(\zeta, 1)}. \quad (\text{A8})$$

The integral over  $d\zeta$  is evaluated

$$\frac{H^\mu}{\Gamma/2\Theta} = 2\pi A - \int_0^{2\pi} d\phi \oint |\mathbf{e}_s \times \mathbf{e}_\rho| \Psi(s;\phi) ds, \quad (\text{A9})$$

where,

$$\Psi(s;\phi) = \begin{cases} 1 + \ln \rho(s;\phi) & \text{if } \rho(s;\phi) > 1 \\ \rho(s;\phi) & \text{if } \rho(s;\phi) \leq 1. \end{cases} \quad (\text{A10})$$

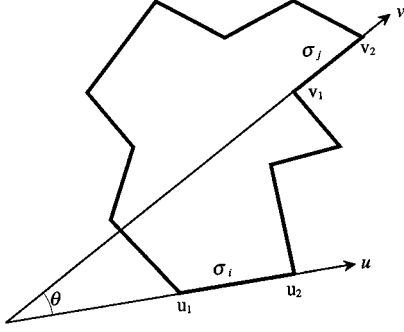


FIG. 17. Coordinate axes used to evaluate each integral term in the summation Eq. (B1). The  $u$  axis is defined to be collinear with the segment  $\sigma_i$  and the  $v$  axis collinear with  $\sigma_j$ . The axes intersect at the origin with angle  $\theta$ .

Finally, the integration over  $d\phi$  is converted to contour integration ( $(d\phi/ds') = [e_\rho \times e_s' / \rho(s, s')]$ )

$$\frac{H^\mu}{\Gamma/2\Theta} = 2\pi A - \oint \oint \frac{\Psi(s, s')}{\rho(s, s')} |e_s \times e_\rho| |e_\rho \times e_{s'}| ds' ds. \quad (\text{A11})$$

## APPENDIX B

This appendix details the analytic evaluation of the electrostatic integral of the Hamiltonian for polygonal domains. For the sake of brevity, however, only evaluation of the indefinite integral will be covered in detail.

Considering the polygon as the set of line segments,  $\{\sigma_1, \sigma_2, \dots, \sigma_N\}$ , the contour integral of Eq. (2.4) is rewritten as a summation of line integrals over the edges of the polygon

$$I = \sum_{i=1}^N \sum_{j=1}^N \int_{\sigma_i} \int_{\sigma_j} \frac{\Psi(s, s')}{\rho(s, s')} |e_s \times e_\rho| |e_\rho \times e_{s'}| ds' ds. \quad (\text{B1})$$

Each integral term in the summation of Eq. (B1) can now be evaluated using (yet another) coordinate transformation. As shown in Fig. 17, two (skew) axes are defined so as to be collinear with the line segments  $\sigma_i$  and  $\sigma_j$  and the origin is defined as the intersection of these two axes. (Note that the following analysis does not hold for parallel  $\sigma_i$  and  $\sigma_j$ , but a simple analogous analysis exists.) These axes, which shall be labeled  $u$  and  $v$ , intersect at angle  $\theta$ . Within this coordinate system,  $\rho$  is found easily through law of cosines,

$$\rho(u, v) = |v\mathbf{e}_v - u\mathbf{e}_u| = \sqrt{u^2 + v^2 - 2uv \cos \theta}, \quad (\text{B2})$$

from which the unit vector  $\mathbf{e}_\rho$  is simply,

$$\mathbf{e}_\rho = \frac{v\mathbf{e}_v - u\mathbf{e}_u}{\rho}. \quad (\text{B3})$$

The unit vectors  $\mathbf{e}_u$  and  $\mathbf{e}_v$  are identical to  $\mathbf{e}_s$  and  $\mathbf{e}_{s'}$ , respectively. In this coordinate system the integral terms of Eq. (B1) can be written as

$$I_{ij} = -\sin^2 \theta \int \int \frac{uv\Psi}{\rho^3} dv du. \quad (\text{B4})$$

Because the definition of  $\Psi$  depends on whether  $\rho$  is greater than or less than unity, two regimes are defined for the evaluation of Eq. (B4). The first regime, which shall be referred to as regime 1, is defined to contain all coordinate pairs  $(u, v)$  for which  $\rho \leq 1$ . The second regime, which shall be referred to as regime 2, contains all  $(u, v)$  for which  $\rho > 1$ . The boundaries between these two regimes follows easily from Eq. (B2). In particular, the limits of regime 1 are  $v^-(u) < v < v^+(u)$ , where

$$v^\pm(u) = u \cos \theta \pm \sqrt{1 - u^2 \sin^2 \theta}. \quad (\text{B5})$$

If  $u \sin \theta > 1$ , then  $\rho$  will be greater than 1—and thus in regime 2—for all  $v$ .

The integral  $I_{ij}$  is first evaluated for regime 1. Substituting the appropriate definition of  $\Psi$ , i.e.,  $\rho$ , into Eq. (B4) yields

$$I_{ij,1} = -\sin^2 \theta \int \int u \int \frac{v}{\rho^2} dv du, \quad (\text{B6})$$

which immediately evaluates to

$$I_{ij,1} = -\sin^2 \theta \int u \ln \rho du - \sin \theta \cos \theta \int u \sin^{-1} \left( \frac{v - u \cos \theta}{\rho} \right) du. \quad (\text{B7})$$

Here the additional subscript on  $I$  indicates that the integration was evaluated in regime 1. In the evaluation of the definite integral, the limits on the integration over  $dv$  can originate from one of two sources: the end points of  $\sigma_j$  or the regime boundary. Therefore, before integrating over  $du$ , Eq. (B7) should be evaluated at the regime boundaries; or else the integration will apply only to constant  $v$ , or the end-points. Substituting Eq. (B5) into  $I_{ij,1}$  produces

$$I_{ij,1}^\pm = \mp \sin \theta \cos \theta \int u \cos^{-1}(u \sin \theta) du. \quad (\text{B8})$$

Here the superscript indicates that  $I_{ij,1}$  was evaluated at either the upper (+) or lower (−) boundary of regime 1.

Finally, Eq. (B7) and Eq. (B8) are integrated over  $du$

$$I_{ij,1} = \frac{u^2 \sin^2 \theta}{4} - \frac{u^2 + v^2}{2} \sin^2 \theta \ln \rho + \frac{v^2 - u^2}{2} \sin \theta \cos \theta \sin^{-1} \left( \frac{v - u \cos \theta}{\rho} \right), \quad (\text{B9})$$

and

$$I_{ij,1}^\pm = \frac{\pm u \cos \theta \sqrt{1 - u^2 \sin^2 \theta}}{4} \mp \frac{2u^2 \sin^2 \theta - 1}{4 \sin \theta} \cos \theta \cos^{-1}(u \sin \theta). \quad (\text{B10})$$

Repeating the above analysis, the integral  $I_{ij}$  is next evaluated for regime 2. The appropriate  $\Psi$ , i.e.,  $1 + \ln \rho$ , is substituted into Eq. (B4)

$$I_{ij,2} = -\sin^2 \theta \int u \int \frac{v(1+\ln \rho)}{\rho^3} dv du, \quad (B11)$$

which evaluates to

$$I_{ij,2} = \int \frac{(u-v \cos \theta)(2+\ln \rho)}{\rho} du + \cos \theta \int \ln(\rho-u \cos \theta+v) du. \quad (B12)$$

Evaluation at the regime boundaries yields

$$I_{ij,2}^{\pm} = 2 \sin^2 \theta \int u du \mp 2 \cos \theta \int \sqrt{1-u^2 \sin^2 \theta} du + \cos \theta \int \ln(1-\sqrt{1 \pm u^2 \sin^2 \theta}) du. \quad (B13)$$

Integrated over  $du$ , Eq. (B12) and Eq. (B13) become, respectively,

$$I_{ij,2} = \rho + \rho \ln \rho + u \ln(\rho-u \cos \theta+v) + v \ln(\rho-v \cos \theta + u) - u \cos \theta, \quad (B14)$$

and

$$I_{ij,2}^{\pm} = u^2 \sin^2 \theta \mp u \cos \theta \sqrt{1-u^2 \sin^2 \theta} + u \cos \theta \ln(1-\sqrt{1-u^2 \sin^2 \theta}) - u \cos \theta. \quad (B15)$$

Evaluation of the definite integral requires no more than determining  $\theta$  and the limiting values of  $u$  and  $v$  for any given  $\sigma_i$  and  $\sigma_j$  and evaluating  $I_{ij}$  at these limits. For segments pairs which reside wholly in a single regime, this is completely straightforward. For segment pairs which extend into both regimes, the integral must first be separated into components which reside in only one regime. For the sake of

computational efficiency, it is useful to examine independently all regime configurations that a pair of segments can possibly exhibit. The number of logarithmic and trigonometric function calls, which tend to be relatively CPU intensive, can thereby be significantly reduced through combination or elimination of terms.

### APPENDIX C

This appendix details the skeletonization process used to determine the number of branches in a domain shape. Geometrically, the medial axis, or skeleton, of a planer shape is the locus of points interior to the shape for which the minimum distance to the perimeter has a degeneracy of 2 or greater [35]. The classic illustration is to imagine a fire lit simultaneously along the entire perimeter of the shape and allowed to burn evenly, the fronts of the fire should meet along the skeleton of the shape [34]. The number of limbs (or branches) in such a skeleton provides one measure for describing the character of domain shape. Because the medial axis cannot, in general, be calculated easily using traditional analytic geometry, the techniques of digital image processing are helpful.

Before the domain shape can be skeletonized, it must be converted to a binary pixel image. The shape is mapped onto a square grid with each element of the grid (or pixel) set to a value of either 1 or 0 depending on whether it represents the interior or exterior of the shape. For convenience, pixels with value 1 will be referred to as belonging to the image. Changing the value of a pixel from 1 to 0 therefore will be referred to as removing the pixel from the image. For the results reported in this paper, the binary image was always 400 pixels by 400 pixels.

In digital image processing, a skeleton, not necessarily the medial axis, is generated through an iteration of selective erosions [34] of the binary image. Each successive image ( $X_i$ ) in the iteration is generated from the preceding ( $X_{i-1}$ ) by filtering, or removing, those pixels whose neighborhood is described by a  $3 \times 3$  pixel mask. For skeletonization, a total of 16 masks are used

$$\begin{aligned} & \begin{bmatrix} 1 & 1 & 1 \\ & 1 & \\ 0 & 0 & 0 \end{bmatrix} \begin{bmatrix} & 1 & 1 \\ 0 & 1 & 1 \\ 0 & 0 & \end{bmatrix} \begin{bmatrix} 0 & & 1 \\ 0 & 1 & 1 \\ 0 & & 1 \end{bmatrix} \begin{bmatrix} 0 & 0 & \\ 0 & 1 & 1 \\ & 1 & 1 \end{bmatrix} \\ & \begin{bmatrix} 0 & 0 & 0 \\ & 1 & \\ 1 & 1 & 1 \end{bmatrix} \begin{bmatrix} & 0 & 0 \\ 1 & 1 & 0 \\ 1 & 1 & \end{bmatrix} \begin{bmatrix} 1 & & 0 \\ 1 & 1 & 0 \\ 1 & & 0 \end{bmatrix} \begin{bmatrix} 1 & 1 & \\ 1 & 1 & 0 \\ & 0 & 0 \end{bmatrix} \\ & \begin{bmatrix} 1 & & 1 \\ & 1 & \\ 0 & 0 & 0 \end{bmatrix} \begin{bmatrix} & 1 & 1 \\ 0 & 1 & 1 \\ 0 & 0 & \end{bmatrix} \begin{bmatrix} 0 & & 1 \\ 0 & 1 & 1 \\ 0 & & 1 \end{bmatrix} \begin{bmatrix} 0 & 0 & \\ 0 & 1 & 1 \\ & 1 & \end{bmatrix} \\ & \begin{bmatrix} 0 & 0 & 0 \\ & 1 & \\ 1 & & 1 \end{bmatrix} \begin{bmatrix} & 0 & 0 \\ 1 & 1 & 0 \\ 1 & & \end{bmatrix} \begin{bmatrix} 1 & & 0 \\ & 1 & 0 \\ 1 & & 0 \end{bmatrix} \begin{bmatrix} 1 & 1 & \\ 1 & 1 & 0 \\ & 0 & 0 \end{bmatrix} \end{aligned} \quad (C1)$$

The entry in the center of the mask represents the pixel in question and the eight surrounding entries represent the eight neighboring pixels. For the mask to fit the neighborhood, all entries of 1 in the mask must correspond to pixels inside the image, all entries of 0 in the mask must correspond to pixels outside the image, and all blank entries may correspond to pixels either inside or outside of the image. Only one mask is used for each iteration. They are used in the order they appear in Eq. (C1). After the final mask has been used, the process repeats beginning with the first mask. Iteration continues until  $X_i$  is identical to  $X_{i-16}$ .

Once the skeleton image ( $X_{sk}$ ) has been created, individual limbs are identified and counted. To identify unique limbs, all triple points of  $X_{sk}$ —pixels which have at least three neighboring pixels in the image—are removed from the image. The resulting image will consist of some number of disconnected limbs. To count the number of branches, each limb (or branch) is recursively removed from the image. Beginning with the first pixel in the image, it and all pixels connected to it by a continuous path are removed. This process of removing limbs is repeated until no pixels remain in the image—the number of repetitions is the number of branches.

- 
- [1] M. Flörsheimer and H. Möhwald, *Chem. Phys. Lipids* **49**, 231 (1989).
- [2] V. Tschärner and H. M. McConnell, *Biophys. J.* **36**, 409 (1981).
- [3] C. M. Knobler, *Science* **249**, 870 (1990).
- [4] A. Miller and H. Möhwald, *J. Chem. Phys.* **86**, 4258 (1987).
- [5] S. A. Langer, R. E. Goldstein, and D. P. Jackson, *Phys. Rev. A* **46**, 4894 (1992).
- [6] A. J. Dickstein, S. Erramilli, R. E. Goldstein, D. P. Jackson, and S. A. Langer, *Science* **261**, 1012 (1993).
- [7] R. E. Rosenweig, *Ferrohydrodynamics* (Cambridge University Press, Cambridge, England, 1982), Chap. 7.
- [8] T. Garel and S. Doniach, *Phys. Rev. B* **26**, 325 (1982).
- [9] R. P. Huebener, *Magnetic Flux Structures in Superconductors* (Springer-Verlag, New York, 1979).
- [10] T. E. Faber, *Proc. R. Soc. London Ser. A* **248**, 460 (1958).
- [11] D. J. Keller, J. P. Korb, and H. M. McConnell, *J. Phys. Chem.* **91**, 6417 (1987).
- [12] H. M. McConnell and V. T. Moy, *J. Phys. Chem.* **92**, 4520 (1988).
- [13] T. K. Vanderlick and H. Möhwald, *J. Phys. Chem.* **94**, 886 (1990).
- [14] M. A. Mayer and T. K. Vanderlick, *Langmuir* **8**, 3131 (1992).
- [15] H. M. McConnell, *J. Phys. Chem.* **94**, 4728 (1990).
- [16] J. M. Deutch and F. E. Low, *J. Phys. Chem.* **96**, 7097 (1992).
- [17] R. E. Goldstein and D. P. Jackson, *J. Phys. Chem.* **98**, 9626 (1994).
- [18] M. A. Mayer and T. K. Vanderlick, *J. Chem. Phys.* **100**, 8399 (1994).
- [19] M. A. Mayer and T. K. Vanderlick, *J. Chem. Phys.* **103**, 9788 (1995).
- [20] M. M. Hurley and S. J. Singer, *J. Phys. Chem.* **96**, 1938 (1992).
- [21] M. M. Hurley and S. J. Singer, *Phys. Rev. B* **46**, 5783 (1992).
- [22] G. C. Barker and M. J. Grimson, *Mol. Phys.* **62**, 269 (1987).
- [23] N. Ostrowsky and J. Peyraud, *J. Chem. Phys.* **77**, 2081 (1982).
- [24] S. Leibler, R. R. P. Singh, and M. E. Fisher, *Phys. Rev. Lett.* **59**, 1989 (1987).
- [25] A. C. Maggs, S. Leibler, M. E. Fisher, and C. J. Camacho, *Phys. Rev. A* **42**, 691 (1990).
- [26] R. E. Norman, G. C. Barker, and T. J. Sluckin, *J. Phys. (France) II* **2**, 1363 (1992).
- [27] T. Kawakatsu, D. Andelman, K. Kawasaki, and T. Taniguchi, *J. Phys. (France) II* **3**, 971 (1993).
- [28] A. C. Maggs and S. Leibler, *Europhys. Lett.* **12**, 19 (1990).
- [29] G. C. Barker and M. J. Grimson, *J. Phys.* **48**, 465 (1987).
- [30] E. Dickinson and S. R. Euston, *J. Chem. Soc. Faraday Trans.* **86**, 805 (1990).
- [31] E. Dickinson and S. R. Euston, *Mol. Phys.* **66**, 865 (1989).
- [32] E. Dickinson and S. R. Euston, *J. Colloid Interface Sci.* **152**, 562 (1992).
- [33] Animated simulation results can be found at <http://asterix.seas.upenn.edu/~mayer/mc>.
- [34] *A Tutorial on Image Processing* (Advanced Imaging Concepts, Princeton, 1992), Chap. 3.
- [35] J. C. Russ, *The Image Processing Handbook* (CRC, Boca Raton, 1992), Chap. 6.
- [36] D. Hearn and M. P. Baker, *Computer Graphics* (Prentice-Hall, Englewood Cliffs, NJ, 1992), Chap. 4.
- [37] D. J. Keller, H. M. McConnell, and V. T. Moy, *J. Phys. Chem.* **90**, 2311 (1986).
- [38] This image was obtained by K. J. Klopfer in the labs of T. K. Vanderlick.
- [39] D. J. Benvegnu and H. M. McConnell, *J. Phys. Chem.* **96**, 6820 (1992).